Journal of Materials Chemistry A

ROYAL SOCIETY OF CHEMISTRY

PAPER

View Article Online
View Journal | View Issue

Cite this: J. Mater. Chem. A, 2022, 10, 2412

Phase formation and performance of solid state reactive sintered $Ce_{0.8}Gd_{0.2}O_{2-\delta}$–$FeCo_2O_4$ composites

Liudmila Fischer,[ab] Kerstin Neuhaus,[c] Christina Schmidt,[c] Ke Ran,[de] Patrick Behr,[a] Stefan Baumann,*[a] Joachim Mayer[de] and Wilhelm A. Meulenberg[ab]

Received 6th July 2021
Accepted 10th October 2021

DOI: 10.1039/d1ta05695f

rsc.li/materials-a

Reactive sintering of dual phase composites for use as oxygen transport membranes is a promising method enabling lower sintering temperatures as well as low-cost raw materials. $Ce_{0.8}Gd_{0.2}O_{2-\delta}$–$FeCo_2O_4$ composites with different nominal weight ratios from 60 : 40 to 90 : 10 are processed by reactive sintering of commercial $Ce_{0.8}Gd_{0.2}O_{2-\delta}$, Fe_2O_3, and Co_3O_4 powders. The phases formed *in situ* during sintering are investigated qualitatively and quantitatively by means of XRD and Rietveld refinement as well as transmission electron microscopy. Besides gadolinia-doped ceria, two Fe/Co-spinel phases are in equilibrium in agreement with the phase diagram. Moreover, a donor-doped $GdFeO_3$-based perovskite $(Gd,Ce)(Fe,Co)O_3$ showing electronic conductivity is formed. Due to these intense phase reactions, the composition of each individual phase is assessed for all composites and their functional properties are discussed. The oxygen permeation performances of the composites are measured including their dependence on temperature and the potential limiting steps are discussed. The results reveal that the phase reactions support the formation of the desired mixed ionic electronic conductivity achieving percolation at low nominal spinel contents. The specific microstructure plays an extremely important role in the membrane performance and, thus, special attention should be paid to this in future research about dual phase membranes.

Introduction

The development of ceramic dual-phase materials for Oxygen Transport Membranes (OTMs) has attracted much attention in the scientific world. These mixed ionic-electronic conductors (MIECs) are operated at elevated temperatures, *i.e.* 700–900 °C, and have the potential for improving the performance and reducing the cost of several industrial gas separation processes due to high energy efficiency.[1,2] If the membrane separates two gas phases with different oxygen partial pressures p_{O_2}, oxygen molecules will be reduced to oxygen ions at the surface of the high p_{O_2}-side taking up in sum four electrons. The ions diffuse through the membrane to the low p_{O_2}-side where they recombine to form oxygen molecules releasing the electrons again. These electrons transfer back to the high p_{O_2}-side simultaneously due to the MIEC character of the membrane material.[3] However, classical single phase MIEC materials, mainly perovskites, suffer from stability issues under operating conditions. Therefore, composite membranes, a combination of both ion and electron conducting ceramic phases, have attracted major interest in recent years.[4–8] Such composites provide the major advantage that two inherently stable materials can be selected provided that their properties such as conductivities, thermal expansion behaviour, and inertness match well. The phase mixture in the composite has to provide separate but continuous pathways for both oxygen ions and electrons and, thus, a percolation of the phases is required. The number of excellent oxygen ion conductors is limited mainly to doped zirconia or ceria, whereby Gd-doped ceria (CGO) shows the highest ionic conductivity in particular at lower temperatures.[9] In contrast, there is a lot of choice of ceramic electronic conductors, which typically crystallize in perovskite or spinel structure both consisting of transition metal elements typically providing electron hole conductivity *via* small polaron hopping.[10–15]

Normally, phases are selected that do not react with each other during sintering and operation in order to maintain these conductive pathways. Recent studies, however, revealed that

[a]Forschungszentrum Jülich GmbH, Institute of Energy and Climate Research, IEK-1 Materials Synthesis and Processing (IEK-1), 52425 Jülich, Germany. E-mail: s.baumann@fz-juelich.de

[b]Faculty of Science and Technology, Inorganic Membranes, University of Twente, 7500 AE Enschede, The Netherlands

[c]Forschungszentrum Jülich GmbH, Institute of Energy and Climate Research, IEK-12, Helmholtz-Institute Münster: Ionics in Energy Storage, Corrensstr. 46, 48149 Münster, Germany

[d]Central Facility for Electron Microscopy GFE, RWTH Aachen University, 52074 Aachen, Germany

[e]Ernst Ruska-Centre for Microscopy and Spectroscopy with Electrons ER-C, Forschungszentrum Jülich GmbH, 52425 Jülich, Germany

CGO mixed with Fe/Co-spinel ($Fe_{3-x}Co_xO_4$) forms an additional orthorhombic perovskite phase during sintering, which even improved the overall performance.[16–18] It turned out that the perovskite phase is $GdFeO_3$-based with Ce and Co on the A-site and B-site, respectively. The Ce^{4+} substituting Gd^{3+} acts as a donor and, thus, electronic conductivity is introduced.[19–22]

This orthorhombic perovskite phase is quite stable and forms distinct grains rather than being a grain boundary phase as speculated in the literature.[10] Obviously, the perovskite phase does not have significant negative effects on the ion- or electron-conducting pathways, *i.e.* ambipolar conductivity. Obviously, this unintended formation of the perovskite phase is not undesired and in contrast might even have positive effects. Lin *et al.*[17] hypothesized an increase in ionic conductivity of the ceria phase due to the extraction of Gd, which otherwise would be segregated at the ceria–ceria grain boundaries resulting in ion transport blocking space charge layers. The maximum performance was observed at a low nominal spinel concentration of 15 wt%,[19] which is well below 30 vol% often referred to as the percolation threshold. However, percolation is affected by many factors[24] in particular in real microstructures. Considering uncorrelated equal-sized spheres in the so-called "swiss-cheese" model the percolation limit is calculated to be 28.95 vol%.[23] Therefore, 30 vol% appears to be a useful guideline although it does not represent a sharp limit. Certain percolating paths can occur well below that. Nevertheless, sufficient electronic conduction requires enough "strong" paths with certain conductivity. On the other hand, the perovskite formation takes place at the expense of the ceria volume fraction reducing oxygen ion conductance, which is considered rate limiting, and increasing the volume fraction of the electronic conducting phases compared to the nominal composition.

Therefore, in order to better understand the influence of the several phases formed during solid state reactive sintering, various nominal combinations of $Ce_{0.8}Gd_{0.2}O_{2-\delta}$ (CGO) and $FeCo_2O_4$ (FCO) are investigated in this work. The resulting phase mixtures are analysed qualitatively and quantitatively based on X-ray diffraction and Rietveld refinement, respectively. Individual phase compositions are determined and their influence on the functional properties, *i.e.* conductivity and oxygen permeance, is discussed.

Experimental

Sample preparation

$Ce_{0.8}Gd_{0.2}O_{2-\delta}$ (CGO), Fe_2O_3 and Co_3O_4 powders were used for the Solid-State Reactive Sintering (SSRS) process. Respective amounts of powders were weighed for nominal CGO-$FeCo_2O_4$ compositions with wt%-ratios of 60 : 40, 65 : 35, 70 : 30, 75 : 25, 80 : 20, 85 : 15 and 90 : 10. The powder mixtures were ball milled in ethanol for 48 h on a roller bench with 175 rpm. After drying in ambient air at 70° the powder mixtures were pressed with a uniaxial press in disc-shaped membranes with $d = 20$ mm. The discs were sintered with a heating rate of 5 K min^{-1} to 1200 °C and a dwell time of 5 hours. At sintering temperature the spinel partially reduces into a high temperature monoxide phase with rocksalt structure. Therefore, a slow rate of 0.5 K min^{-1} between 900 and 800 °C is implemented in the cooling cycle in order to ensure complete reoxidation of the high temperature Co/Fe-monoxide phase to the spinel phase stable at operating temperatures according to the $Fe_{3-x}Co_xO_4$ phase diagram.[16]

The sintered discs were ground to approx. 1 mm thickness in 2 steps (by WS FLEX 18C) with SiC papers of P 800 and P 1200 grit, respectively. Subsequently, porous LSCF ($La_{0.58}Sr_{0.4}Co_{0.2}Fe_{0.8}O_{3-\delta}$) catalytic activation layers with a thickness of approx. 5 μm were applied *via* screen printing on both sides of the discs and calcined at 1100 °C for 5 hours.

Single-phase powders of spinel as well as the resulting perovskite, *i.e.* $Gd_{0.85}Ce_{0.15}Fe_{0.75}Co_{0.25}O_3$, were synthesized by gelation and complexation of an aqueous solution of metal nitrates known as the Pechini-method.[25]

Characterization methods

Crystal structure. The crystal structures are determined *via* X-ray diffraction (XRD) using a D4 ENDEAVOR (Bruker, Germany). The diffraction angle is varied in the range of 10° to 80° 2θ with increments of 0.02° 2θ and 0.75 seconds of measurement time per step. Measured data were analysed with help of the program package X'Pert HighScore (PANalytical B.V., version 3.0.5). Crystal structure analysis and associated phase quantifications were carried out by Rietveld refinement using the software Profex (Version 4.2.2). The errors of each fitting are calculated individually and given in Table 1.

Microscopy. The morphology of the materials is analysed by Scanning Electron Microscopy (SEM) and Energy Dispersive X-ray Spectroscopy (EDS). The SEM images with different magnifications are taken with Zeiss Ultra 55 and Zeiss Supra 50 VP1 (Carl Zeiss NTS GmbH, Germany) equipment. The electronic conductivity of the samples was enhanced by sputter deposition of a thin platinum layer prior to the analysis.

TEM specimens were cut from the CGO-FCO pellets by focused ion beam (FIB) milling using an FEI Strata 400 system with a Ga ion beam. Further thinning and cleaning were performed with an Ar ion beam in a Fischione Nanomill 1040 at 900 eV and 500 eV beam energy respectively. TEM, energy-filtered TEM imaging and electron diffraction were performed using an FEI Tecnai F20 at 200 kV. High-resolution high-angle annular dark-field (HAADF) imaging was conducted with an FEI Titan G2 80-200 ChemiSTEM microscope equipped with an XFEG and a probe Cs corrector.[26]

Electrical conductivity. The total conductivity of the single-phase perovskite samples was determined by an analysis of temperature dependent impedance spectra using a Novotherm HT 1200 frequency analyzer. The samples were coated with a Pt resinate paste (RP 070107, Heraeus GmbH, Germany) and Pt sheet contacts were attached at both sides of the sample. The samples were measured in air. An AC voltage peak-to-peak amplitude of 40 mV was applied for all measurements. As the electronic conductivity of all composites was very high, no splitting in separate contributions from the grain bulk and grain boundary was possible, and only a straight line (ohmic resistor) was visible in the Nyquist plots. The temperature

Table 1 Lattice parameter and weight fraction F of the phases of the CGO-FCO composites with a nominal FCO content of 10–40 wt% sintered at 1200 °C for 5 h. The space groups of the phases are given in the headline. Numbers in square brackets give the calculated uncertainty of the last digit

	Fluorite (CGO) $Fm\bar{3}m$		Fe-rich spinel $Fd3m$		Co-rich spinel $Fd3m$		Perovskite (GCFCO) $Pnma$			
								Lattice parameter [Å]		
FCO [wt%]	F [wt%]	$a = b = c$ [Å]	F [wt%]	$a = b = c$ [Å]	F [wt%]	$a = b = c$ [Å]	F [wt%]	a	b	c
10	82.1[3]	5.4213[5]	0	—	7.1[3]	8.1309[2]	10.7 [2]	5.3370[3]	5.6121[4]	7.6467[8]
15	73.5[3]	5.4215[5]	7.8[2]	8.2483[8]	5.1[2]	8.1321[3]	13.6[2]	5.3376[4]	5.6147[5]	7.6492[8]
20	69.4[3]	5.4221[4]	4.2[2]	8.2426[9]	14.5[2]	8.1795[2]	11.9[2]	5.3421[4]	5.6191[4]	7.6583[7]
25	62.5[3]	5.4227[5]	9.2[2]	8.3032[8]	13.3[2]	8.1436[2]	12.9[2]	5.3404[3]	5.6163[4]	7.6549[7]
30	61.3[3]	5.4220[4]	15.5[2]	8.2994[8]	11.8[2]	8.1490[2]	11.4[2]	5.3399[3]	5.6141[5]	7.6576[8]
35	56.3[3]	5.4201[4]	16.4[2]	8.2967[8]	17.0[2]	8.1580[2]	10.3[2]	5.3409[3]	5.6121[4]	7.6368[8]
40	51.7[3]	5.4211[5]	20.3[2]	8.2966[9]	18.2[2]	8.1461[3]	9.8[2]	5.3395[3]	5.6121[4]	7.6410[8]

dependent electronic conductivity of the composites was measured using a DC measurement setup (Keithley 2600B): the top of the sample pellet was in contact with a Pt micro contact with a diameter of about 200–400 nm and the bottom was in contact with a Pt sheet. Additionally, Pt resinate paste (RP 070107, Heraeus GmbH) was applied on the sheet to reduce the contact resistance. The exact size of the micro contact was determined by measuring its imprint on the sample after the measurements using light microscopy and comparing it with light microscopy images of the contact itself.

In order to distinguish the oxygen partial pressure dependent electronic conductivity contribution from the total conductivity, Hebb–Wagner measurements[27,28] were conducted. The Pt micro contact described above was additionally surrounded by a gas tight encapsulation (IP 041 glass paste by Heraeus GmbH), using the same measurement setup as for the standard DC measurements.

The experimental error of both methods is ±5%.

Oxygen permeation measurements. The oxygen permeation experiments were performed in a vertical quartz glass housing, where the membranes were sealed with two gold rings with an inner diameter of 13 mm. The separation of the oxygen from ambient air fed with 250 ml_N min^{-1} was performed between approx. 650 °C and 1000 °C by using argon as a sweep gas with 50 ml_N min^{-1} flow rate using mass flow controllers (Bronkhorst, Germany). The oxygen and nitrogen concentration in the permeate gas, *i.e.* oxygen enriched argon, was detected with a mass spectrometer (Omnistar, Pfeiffer Vacuum GmbH, Germany). With help of the measured nitrogen concentration air leakage through the membrane or the sealing is considered using

$$j_{O_2} = F_{Ar}\left(\frac{X_{O_2} - \frac{1}{4}X_{N_2}}{1 - X_{O_2} - X_{N_2}}\right)\frac{1}{A_{mem}} \quad (1)$$

with F_{Ar} being the argon flow rate, *i.e.* 50 ml_N min^{-1}, X_{O_2} and X_{N_2} the oxygen and nitrogen concentration in the permeate gas, respectively, and A_{mem} the open membrane area, *i.e.* 1.33 mm^2. The factor $\frac{1}{4}$ reflects the O_2/N_2 ratio in the air feed assuming that the leak is not gas selective.

Since the oxygen partial pressure in the permeate gas is temperature dependent, the driving force of the permeation rate is not constant during the measurement. Moreover, the sample thickness after grinding has a deviation from the target, *i.e.* 1 mm, of ±8%. Therefore, the permeance, *i.e.* driving force normalized permeation rate, normalized to the reference thickness $L_0 = 1$ mm is calculated assuming Wagner behaviour using

$$\text{Permeance} = \frac{j_{O_2}}{\ln\frac{p'_{O_2}}{p''_{O_2}}}\frac{L_{mem}}{L_0} \quad (2)$$

with p'_{O_2} and p''_{O_2} being the oxygen partial pressures in the retentate and permeate gas, respectively, and L_{mem} the actual membrane thickness.

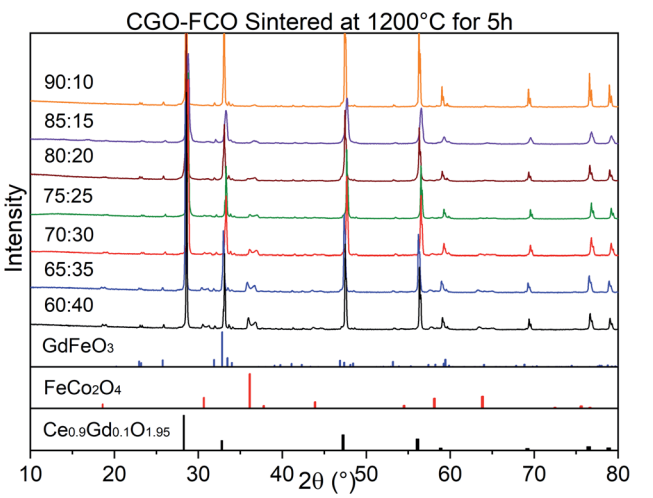

Fig. 1 XRD patterns of the CGO-FCO composites in a row with various FCO contents sintered at 1200 °C for 5 h. At the bottom, reference reflections are shown for the perovskite (01-072-9909) in blue, spinel (01-074-3417) in red, and fluorite (01-075-0161) in black. ICCD numbers are given in brackets.

The overall experimental error cannot be calculated precisely. It is assumed to be ±10%, which is well accepted in the literature.

Results and discussion

Microstructure

The phase identification has been performed *via* XRD. All samples consist of ceria ($Ce_{0.8}Gd_{0.2}O_{2-\delta}$) and spinel-type ($FeCo_2O_4$) phases with the additional orthorhombic perovskite structure $GdFeO_3$ as expected without the formation of any other phases, Fig. 1. The change in the spinel fraction in the composite is evident by the decrease of the intensities of the corresponding reflections in the XRD patterns in the region of $35 \leq 2\theta \leq 38°$. Moreover, reflection splitting is visible revealing two coexisting spinel phases in accordance with the phase diagram.[16] The phases are homogeneously distributed as indicated in Fig. 2. The three crystallographic phases are confirmed as fluorite ($Ce_{1-x}Gd_xO_2$), spinel ($Fe_{3-x}Co_xO_4$) and perovskite ($GdFeO_3$) and exemplarily shown by the HAADF images in Fig. 3 for the 60 : 40 CGO-FCO composite. The weight fractions and lattice parameters of each phase were determined by Rietveld refinement as shown in Table 1. In agreement with the phase diagram of the $Fe_xCo_{3-x}O_4$ system two types of spinel are present in the range of $0.65 \leq Fe \leq 1.07$, *i.e.* Co-rich (normal spinel) and Fe-rich (inverse spinel). Indeed, both spinels are detected for all composites except 90 : 10 proportion, in which only of the Co-rich normal spinel is found. The resulting weight fraction of each phase is plotted *versus* the nominal spinel content in Fig. 4.

As expected, the CGO weight fraction after sintering steadily decreases with increasing nominal FCO content in the primary

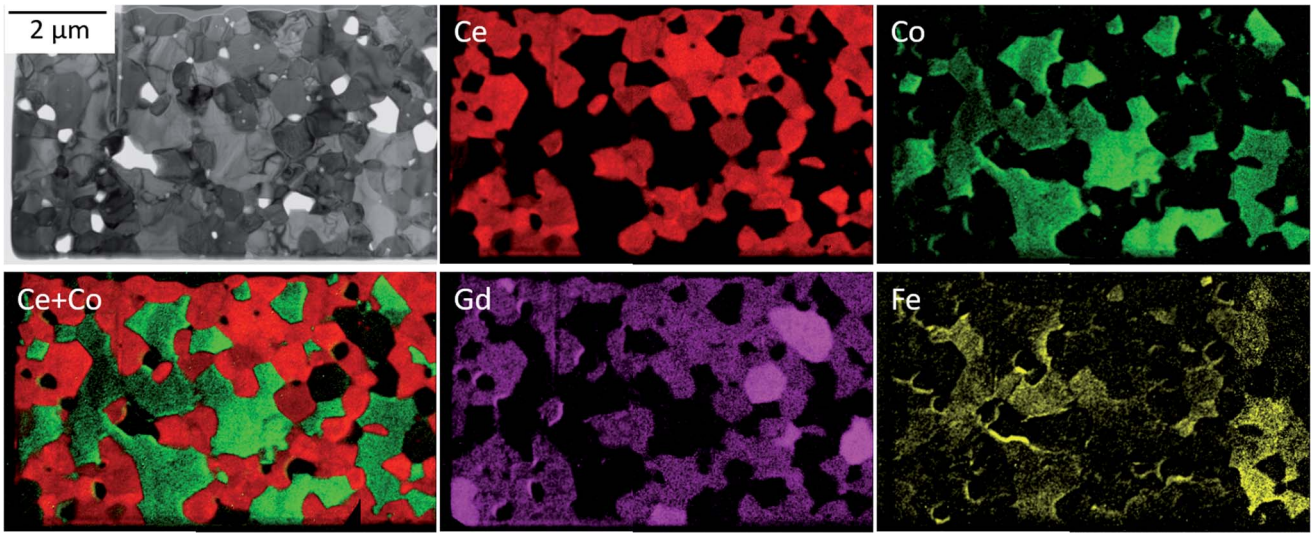

Fig. 2 Energy-filtered TEM (EFTEM) analysis identifying three main phases: Gd-doped ceria (red), Fe/Co-oxide (green) and the $GdFeO_3$-based perovskite (bright magenta).

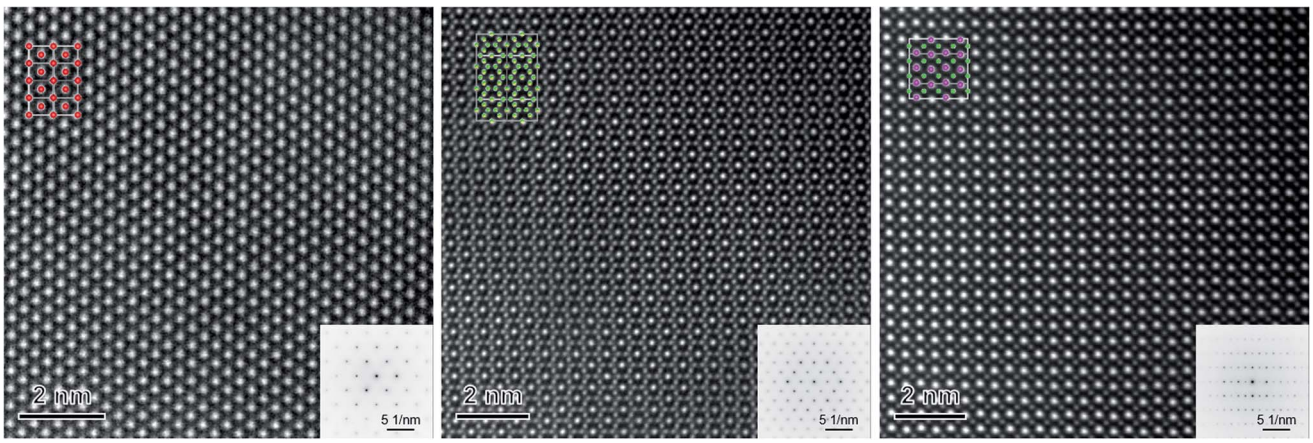

Fig. 3 High-resolution HAADF images of single grains of CGO (left), FCO (middle) and GCFCO (right) recorded along the [101], [101] and [110] zone axis, respectively. Upper left/lower right insets are the corresponding structural models/diffraction patterns measured in the TEM mode. Oxygen is not shown.

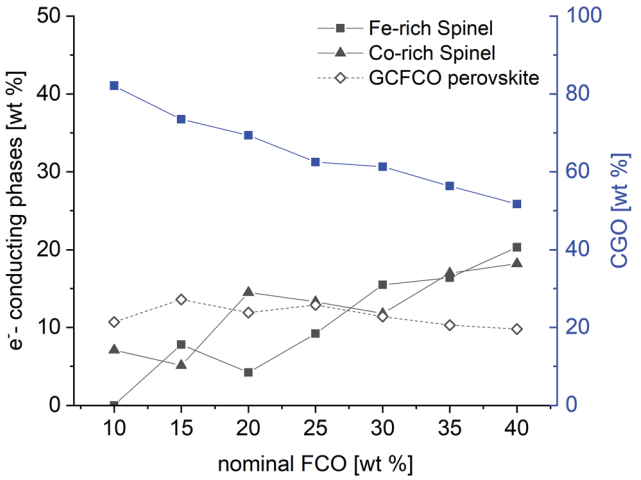

Fig. 4 Weight fraction of detected phases in the CGO-FCO composites sintered at 1200 °C for 5 h according to Table 1.

Table 2 Fe- and Gd-content in spinel and fluorite phases, respectively, after reactive sintering

Nominal spinel content [wt%]	x in $Co_{3-x}Fe_xO_4$ Fe-rich spinel	x in $Co_{3-x}Fe_xO_4$ Co-rich spinel	x in $Ce_{2-x}Gd_xO_{2-d}$
10	—	0.14	0.15
15	0.97	0.15	0.152
20	0.92	0.48	0.162
25	1.34	0.23	0.17
30	1.32	0.27	0.16
35	1.30	0.33	0.13
40	1.30	0.25	0.146

powder mixture, whereas the weight fraction of both spinel phases increases. In contrast, the perovskite phase weight fraction remains relatively constant in the range of 11 ± 2% for all composites. However, due to the intense phase interactions the chemical compositions of the respective phases change, which is reflected by a change in lattice parameters in Table 1.

Phase composition

The exact chemical composition of the different phases in the sintered composite is not accessible with methods such as EDS.

Therefore, lattice parameters are used to determine the chemical composition of all detected phases after sintering.

Spinel and fluorite phases. The spinel system $Fe_xCo_{3-x}O_4$ with *Fd*3*m* structure can be well analysed with the help of Vegard's law.[29] According to this rule of mixtures the linear relationship between the Fe-content and lattice parameter is given in that binary solid solution. The resulting Fe-content in the spinel phases is listed in Table 2. In contrast, the fluorite structure of $Ce_{1-x}Gd_xO_{2-x/2}$ does not obey Vegard's law[30] although there is a nearly linear relationship between the lattice parameter and Gd-content x in the region of interest, *i.e.* $x \leq 0.2$.

Table 3 Calculated composition of the $Gd_{1-x}Ce_xFe_{1-y}Co_yO_3$ perovskite phase after reactive sintering

Nominal spinel content [wt%]	Gd	Ce	Fe	Co
10	0.61	0.39	0.68	0.33
15	0.58	0.42	0.69	0.31
20	0.50	0.50	0.58	0.42
25	0.43	0.57	0.42	0.58
30	0.52	0.48	0.42	0.58
35	0.75	0.25	0.41	0.59
40	0.63	0.37	0.45	0.55

Hong and Virkar[31] derived an equation for the lattice parameter of doped ceria considering the ionic radii of the different components

$$a = \frac{4}{\sqrt{3}}[xr_M + (1-x)r_{Ce} + (1-0.25x)r_o + 0.25xr_{Vo}]0.9971$$

where x is the concentration of the dopant in pure CeO_2, here Gd, so $r_M = r_{Gd} = 0.1053$ nm, $r_{Ce} = 0.097$ nm is the radius of the cerium ion, $r_o = 0.138$ nm and $r_{Vo} = 0.1164$ is the radius of the oxygen ion and vacancy, respectively. The resulting Gd-content x is listed in Table 2.

Perovskite phase. The $Gd_{1-x}Ce_xFe_{1-y}Co_yO_3$ system is much less investigated and, thus, the determination of the perovskite composition from the lattice parameter is not reliable. Therefore, it is calculated assuming a constant mass of the respective cations, *i.e.* no significant evaporation or similar effects occur during sintering. A mass balance is done using cation stoichiometry used for the synthesis and the calculated amount and composition of spinels and fluorite after sintering, Table 3.

Composite composition

With knowledge of the composition and weight fraction of the individual phases the actual volume fractions of those coexisting phases can be calculated. The required densities of the

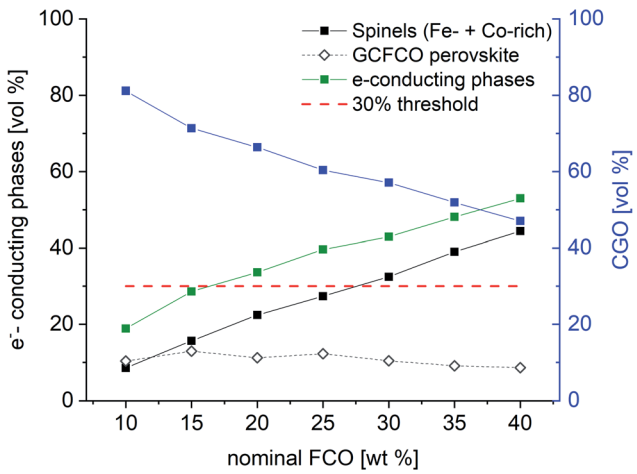

Fig. 5 Volume fraction of detected phases in the CGO-FCO composites sintered at 1200 °C for 5 h.

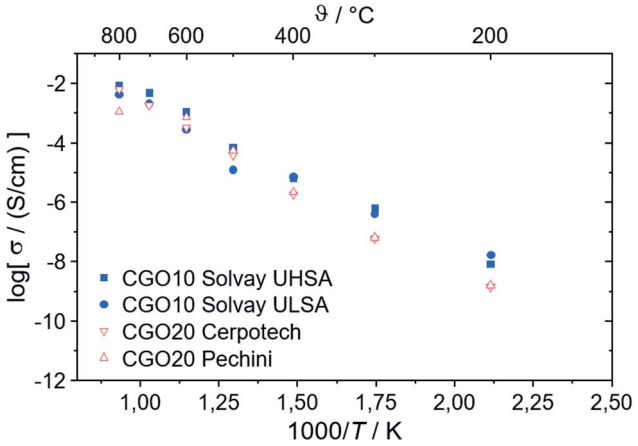

Fig. 6 Ionic conductivity of CGO with 10 and 20 mol% Gd-substitution, respectively. The experimental error is ±5%.

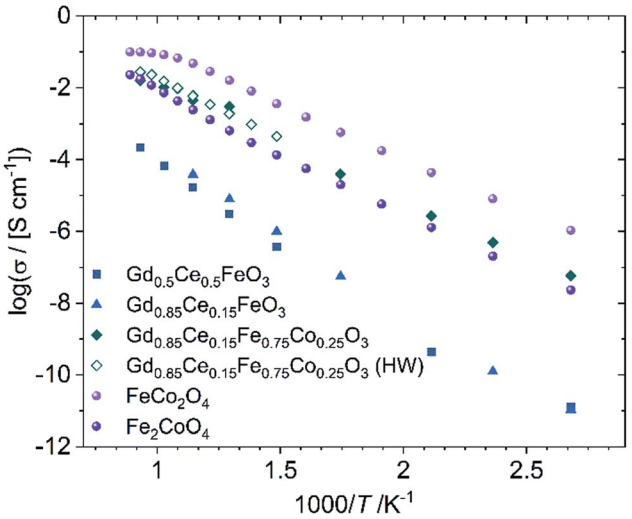

Fig. 7 Electronic conductivity of phases identified in the composite. The legend gives nominal compositions, because some samples are not single phase. The experimental error is ±5%.

different phases are calculated for each composite individually using

$$\frac{M_f Z N_A}{V_c} \quad (3)$$

with M_f being the molecular weight of one formula unit according to Tables 2 and 3, Z the number of formula units per unit cell, N_A the Avogadro constant, and V_c the unit cell volume according to the lattice parameters given in Table 1. The average densities in g cm^{-3} are 5.55 ± 0.064, 5.89 ± 0.041, 7.22 ± 0.005, and 7.39 ± 0.059 for the Fe-rich spinel, Co-rich spinel, fluorite, and perovskite, respectively, revealing only gradual changes of the density with composition. Fig. 5 shows the volume fraction of the fluorite, perovskite and spinel phases *versus* the nominal weight fraction of FCO in the initial powder mixture. Indeed, there is a linear dependence of the total spinel amount, which exceeds the percolation threshold, *i.e.* 30 vol%, above 30 wt% nominal FCO content. Since the perovskite phase contributes to the electronic conductivity the cumulative volume fraction of all electronic conducting phases is plotted, too. This volume fraction already exceeds the percolation threshold >15 wt% nominal spinel content. This explains the excellent performance of the composite at low nominal FCO contents. Nevertheless, even below that threshold significant oxygen permeation can be measured down to 10% nominal spinel content, *i.e.* 18 vol% electronic conducting phases.

Performance

Individual phases. The phase changes during reactive sintering need to be considered to assess the composite performance. For $Ce_{1-x}Gd_xO_{2-x/2}$ it is well known that the ionic conductivity is hardly affected for $0.1 \leq x \leq 0.2$. This is confirmed by own measurements of different CGO powders, Fig. 6.

In contrast, the chemical composition of the electronic conducting phases determines their conductivities. Two spinels are synthesized exemplarily, *i.e.* Fe_2CoO_4 and $FeCo_2O_4$. Fig. 7 shows that the Fe-richer spinel shows lower conductivity. According to Table 2, the maximum Fe-content in the spinel phases is 1.34, well below that of Fe_2CoO_4 and, thus, the electronic conductivity can be regarded as sufficiently high. In the perovskite system single phase $Gd_{0.85}Ce_{0.15}Fe_{0.75}Co_{0.25}O_3$ (GCFCO) shows very similar conductivity, Fig. 7. Hebb–Wagner measurements of the electronic partial conductivities with variable p_{O_2} of this perovskite (exemplarily shown for $p_{O_2} = 0.21$ bar as open symbols in Fig. 7) showed a similar dimension like the total conductivities from impedance spectroscopy. In addition, oxygen permeation was negligible, *i.e.* below the detection limit, revealing that the chosen GCFCO is a pure electronic conductor and does not possess significant oxygen non-stoichiometry, *i.e.* $\delta \approx 0$. Moreover, Hebb–Wagner measurements down to $p_{O_2} = 10^{-10}$ bar did not show any

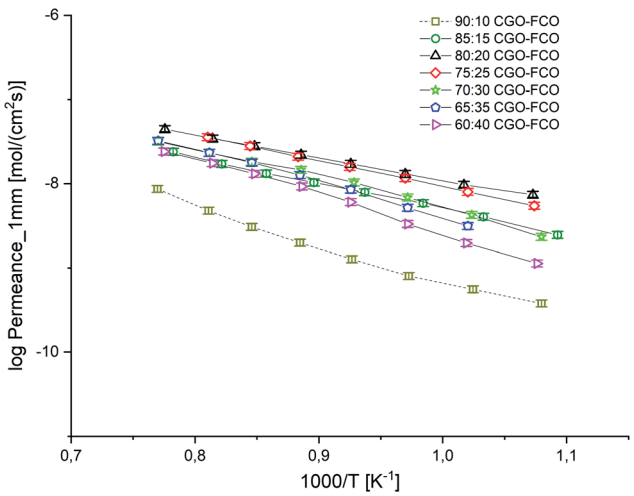

Fig. 8 Arrhenius plot of the permeance of CGO-FCO composites normalized to a thickness of 1 mm. Error bars represent ± 10% of the measured values.

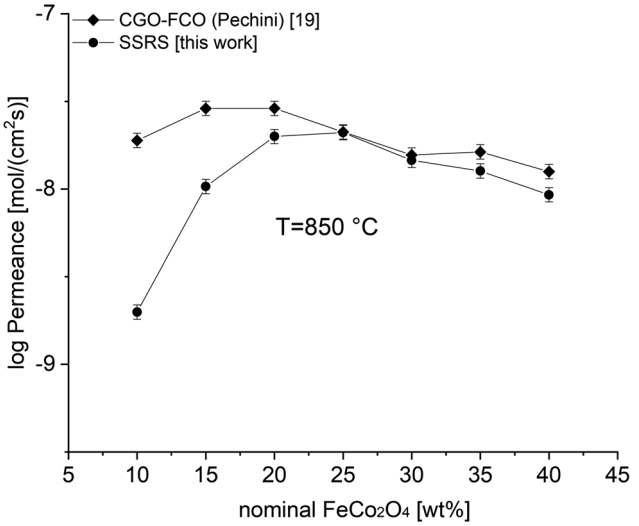

Fig. 9 Permeance of differently synthesized composites depending on the nominal FCO-content. Error bars represent ± 10% of the measured values.

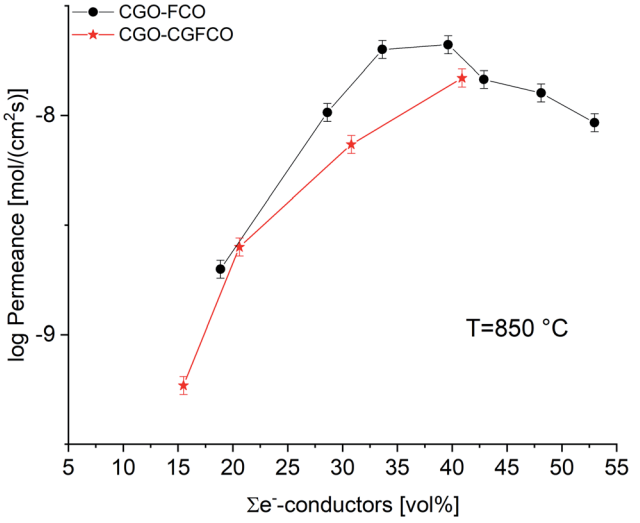

Fig. 11 Permeance of CGO-FCO and CGO-GCFCO composites depending on the volume fraction of e^--conducting phases. Error bars represent ±10% of the measured values.

change of transport mechanisms indicating that the non-stoichiometry remains close to zero in that p_{O_2}-range.

Co-free perovskites, in contrast, show very low conductivities. However, these materials did not show phase purity, but additional phases such as Gd-doped ceria, magnetite, and $Gd_3Fe_5O_{12}$, which are not present in the composites. Apparently, Co substitution on the B-site of $GdFeO_3$ supports perovskite phase formation. Ce substitution on the A-site acts as the donor and enables electronic conductivity. The $GdFeO_3$-based perovskites detected in the composites show Co- and Ce-substitution of 31–59% at the B-site and 25–57% at the A-site, respectively, Table 3. Therefore, those phases are considered as good electronic conductors.

Composites. The composites show good performance, Fig. 8, as expected from previous reports.[19] For better comparison the oxygen permeance is normalized to the membrane thickness according to eqn (2). As a result, the activation energy E_A of the permeance is equal to that of the ambipolar conductivity. Data from Fig. 8 reveal an E_A of 60–80 kJ mol^{-1} indicating that the ionic conductivity of the ceria phase is rate limiting. Only for the composite with nominal composition 90 : 10 wt% E_A = 101 kJ mol^{-1} indicating a change in the rate limiting process probably due to the lack of electronic conductivity.

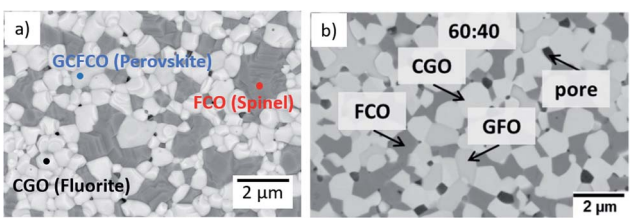

Fig. 10 Microstructure of a sintered 60 : 40 CGO-FCO composite (a) synthesized by SSRS (SEM of surface, this work) and (b) synthesized by the Pechini method previously (SEM cross-section. Reproduced with permission.[19] Copyright 2017, Elsevier).

Fig. 9 shows a comparison of this work with previously reported data on composites of the same nominal compositions, but differently synthesized, *i.e.* by the Pechini method,[19] a sol–gel technique starting from an aqueous precursor solution. The permeance follows the same systematic process. However, the Pechini synthesized composites show higher performance for low FCO-contents. This might be attributed to the typically finer microstructure with highly homogeneous cation distribution achieved by the sol–gel synthesis. Even if there are some percolating paths, these need to be "strong" enough to ensure sufficient electronic conduction. The comparison of microstructures (Fig. 10) indicates similarly small ceria grains in the sub-micron range and slightly coarser spinel agglomerates for SSRS compared to that obtained by the Pechini method and, thus, no drastic difference. Unfortunately, quantification is not possible due to the low differences in grey scale contrast between the several phases.

But, as analysed above the phase interactions during sintering lead to an increase in electronic conducting phases. However, this takes place at the expense of the ceria content, *i.e.* ionic conducting volume, which is rate limiting and thus not desired. Fig. 11 shows the permeance *versus* the volume fraction of the sum of electronic conducting phases. In comparison to the CGO-FCO series CGO-GCFCO composites were synthesized using commercially available CGO and pre-synthesized $Gd_{0.85}Ce_{0.15}Fe_{0.75}Co_{0.25}O_3$. In this case no phase interactions during sintering are observed and, thus, indeed dual phase membranes are achieved. At low and high e^--conductor content, respectively, the permeance is quite similar. Above 40 vol% an identical behaviour can be expected because the ionic conductivity, *i.e.* ceria content, is the rate limiting factor. Around 30 vol% of e^--conductor content the SSRS CGO-FCO series shows higher performance over the CGO-GCFCO series. This, again, reveals the importance of the phase distribution, *i.e.* microstructure, inside the composite close to the percolation threshold. It seems to be even more important than the

phase itself, in this case perovskite or spinel, or actually both together, as long as the electronic conductivity of these individual phases is sufficiently high.

Conclusions

MIEC composites with nominal composition $Ce_{0.8}Gd_{0.2}O_{2-\delta}$ (CGO) – $FeCo_2O_4$ (FCO) can be successfully synthesized by the cost-efficient solid state reactive sintering (SSRS) technique using commercial powders of CGO as well as Fe_2O_3 and Co_3O_4. During sintering several phase interactions occur resulting in a mixture of four phases after sintering, *i.e.* CGO, two Fe/Co-spinel phases and a $GdFeO_3$-based perovskite. The composition of the individual phases depends on the nominal CGO-FCO ratio defining the mixture of the raw powders. Nevertheless, their functional characteristics, *i.e.* ionic or electronic conductivity, remain. For the perovskite formation during reactive sintering approx. 5 mol% of Gd is extracted from the initial CGO, which does not affect its ionic conductivity significantly. But, the ceria volume fraction is reduced and, thus the ion conducting pathways. The two spinel phases are in equilibrium according to the $Fe_{3-x}Co_xO_4$ phase diagram and provide electronic conductivity, just like the perovskite $Gd_{1-x}Ce_xFe_{1-y}Co_yO_3$, which is a donor doped $GdFeO_3$ and, thus, a pure electronic conductor with a similar conductivity to the spinel. Consequently the electronic conducting volume fraction is increased.

In MIEC composites typically the ionic conductivity is rate limiting provided that sufficient electronic conduction is achieved, which is a combination of the electronic conductivity of the selected phase(s) and the presence of sufficient percolating paths. This represents a typical optimization task, *i.e.* maximizing the ionic conducting volume without losing percolation of the electronic conduction.

In comparison to a two phase system without reactive sintering made from pre-synthesized CGO and GCFCO ($Gd_{0.85}Ce_{0.15}Fe_{0.75}Co_{0.25}O_3$) the CGO-FCO SSRS shows higher performance close to 30 vol% of the electronic conducting phases, which is often considered as the percolation threshold. The phase interactions during SSRS obviously help achieving significant percolation of electronic conductors at high ceria content enhancing ambipolar conductivity compared to the CGO-GCFCO series solid state sintered without phase reactions. In the Pechini synthesized CGO-FCO series reported previously comparable phase interactions as in SSRS series occur. Even higher performance at the same nominal composition close to that percolation threshold was found, which might be attributed to the finer particles synthesized by the Pechini method. Moreover, the potential role of grain boundaries needs more attention. These results reveal the importance of tailoring the microstructure of composite membranes by materials engineering, which seems to be even more important compared to the investigation of more and more novel material mixtures.

Summarizing, SSRS of CGO-FCO is an attractive route – even though slightly less performing compared to the Pechini synthesized variant – due to its suitability for industrialization using cheap and abundant oxides. Further developments should concentrate on tailoring the resulting microstructure closing the gap with the Pechini synthesized composites.

Nevertheless, the *in situ* formed perovskite system (GdCe)$(FeCo)O_3$ represents an interesting alternative candidate as an electronic conductor in ceria-based composite membranes. It is expected to provide higher chemical stability compared to FCO in particular at lower p_{O_2}. Moreover, there might be a chance to introduce oxygen non-stoichiometry, which would lead to mixed conductivity supporting ionic transport and facilitating surface exchange not investigated here. Therefore, the GCFCO system should be further investigated.

Author contributions

Liudmila Fischer: investigation & writing – original draft, Kerstin Neuhaus: funding acquisition, investigation, project administration & writing – original draft, Christina Schmidt: investigation & writing – original draft, Ke Ran: investigation & writing – original draft, Patrick Behr: investigation, Stefan Baumann: conceptualization, investigation, funding acquisition & writing – original draft, Joachim Mayer: funding acquisition, & writing – review & editing, Wilhelm A. Meulenberg: resources, supervision & writing – review & editing.

Conflicts of interest

There are no conflicts to declare.

Acknowledgements

The work is funded by the Deutsche Forschungsgemeinschaft (DFG, German Research Foundation) – 387282673.

References

1 W. Deibert, M. E. Ivanova, S. Baumann, O. Guillon and W. A. Meulenberg, *J. Membr. Sci.*, 2017, **543**, 79–97.
2 A. A. Plazaola, A. C. Labella, Y. Liu, N. B. Porras, D. A. P. Tanaka, M. V. S. Annaland and F. Gallucci, *Processes*, 2019, **7**(3), 128.
3 J. Sunarso, S. Baumann, J. M. Serra, W. A. Meulenberg, S. Liu, Y. S. Lin and J. C. Diniz da Costa, *J. Membr. Sci.*, 2008, **320**, 13–41.
4 M. Balaguer, J. García-Fayos, C. Solís and J. M. Serra, *Chem. Mater.*, 2013, **25**, 4986–4993.
5 H. Cheng, N. Zhang, X. Xiong, X. Lu, H. Zhao, S. Li and Z. Zhou, *ACS Sustainable Chem. Eng.*, 2015, **3**, 1982–1992.
6 H. Luo, T. Klande, Z. Cao, F. Liang, H. Wang and J. Caro, *J. Mater. Chem. A*, 2014, **2**, 7780–7787.
7 S. Cheng, M. Søgaard, L. Han, W. Zhang, M. Chen, A. Kaiser and P. V. Hendriksen, *Chem. Commun.*, 2015, **51**, 7140–7143.
8 J. Garcia-Fayos, M. Balaguer and J. M. Serra, *ChemSusChem*, 2015, **8**, 4242–4249.
9 J. A. Kilner and M. Burriel, *Annu. Rev. Mater. Res.*, 2014, **44**, 365–393.
10 H. Takamura, T. Kobayashi, T. Kasahara, A. Kamegawa and M. Okada, *J. Alloys Compd.*, 2006, **408–412**, 1084–1089.

11 H. Luo, H. Jiang, K. Efimov, F. Liang and H. Wang, *Ind. Eng. Chem. Res.*, 2011, **50**, 13508–13517.
12 W. Fang, F. Liang, Z. Cao, F. Steinbach and A. Feldhoff, *Angew. Chem., Int. Ed.*, 2015, **54**, 4847–4850.
13 U. Pippardt, J. Böer, C. Bollert, A. Hoffmann, M. Heidenreich, R. Kriegel, M. Schulz and A. Simon, *J. Ceram. Sci. Technol.*, 2014, **5**, 309–316.
14 J. Garcia-Fayos, V. B. Vert, M. Balaguer, C. Solís, C. Gaudillere and J. M. Serra, *Catal. Today*, 2014, **257**, 221–228.
15 Y. He, L. Shi, F. Wu, W. Xie, S. Wang, D. Yan, P. Liu, M. R. Li, J. Caro and H. Luo, *J. Mater. Chem. A*, 2017, **6**, 84–92.
16 M. Ramasamy, S. Baumann, J. Palisaitis, F. Schulze-Küppers, M. Balaguer, D. Kim, W. A. Meulenberg, J. Mayer, R. Bhave, O. Guillon and M. Bram, *J. Am. Ceram. Soc.*, 2016, **99**(1), 349–355.
17 Y. Lin, S. Fang, D. Su, K. S. Brinkman and F. Chen, *Nat. Commun.*, 2015, **6**, 6824.
18 Z. Zhang, W. Zhou, Y. Chen, D. Chen, J. Chen, S. Liu, W. Jin and Z. Shao, *ACS Appl. Mater. Interfaces*, 2015, **7**, 22918–22926.
19 M. Ramasamy, E. S. Persoon, S. Baumann, M. Schroeder, F. Schulze-Küppers, D. Görtz, R. Bhave, M. Bram and W. A. Meulenberg, *J. Membr. Sci.*, 2017, **544**, 278–286.
20 F. Zeng, J. Malzbender, S. Baumann, A. Nijmeijer, L. Winnubst, M. Ziegner, O. Guillon, R. Schwaiger and W. A. Meulenberg, *J. Eur. Ceram. Soc.*, 2021, **41**, 509–516.
21 F. Zeng, J. Malzbender, S. Baumann, M. Krüger, L. Winnubst, O. Guillon and W. A. Meulenberg, *J. Eur. Ceram. Soc.*, 2020, **40**, 5646–5652.
22 F. Zeng, S. Baumann, J. Malzbender, A. Nijmeijer, L. Winnubst, O. Guillon, R. Schwaiger and W. A. Meulenberg, *J. Membr. Sci.*, 2021, **628**, 119248.
23 C. D. Lorenz and R. M. Ziff, *J. Chem. Phys.*, 2001, **114**, 3659–3661.
24 S. C. van der Marck, *Phys. Rev. E: Stat. Phys., Plasmas, Fluids, Relat. Interdiscip. Top.*, 1997, **55**, 1514–1517.
25 K. Schmale, M. Grünebaum, M. Janssen, S. Baumann, F. Schulze-Küppers and H.-D. Wiemhöfer, *Phys. Status Solidi B*, 2011, **248**(2), 314–322.
26 A. Kovács, R. Schierholz and K. Tillmann, *J. Large-Scale Res. Facil.*, 2016, **2**, 68–71.
27 A. Buchheit, B. Teßmer, K. Ran, J. Mayer, H.-D. Wiemhöfer and K. Neuhaus, *ECS J. Solid State Sci. Technol.*, 2019, **8**, P41–P50.
28 K. Neuhaus, R. Dolle and H.-D. Wiemhöfer, *J. Electrochem. Soc.*, 2018, **165**, F533–F542.
29 N. Bahlawane, P. H. T. Ngamou, V. Vannier, T. Kottke, J. Heberle and K. Kohse-Höinghaus, *Phys. Chem. Chem. Phys.*, 2009, **11**, 9224–9232.
30 C. Artini, M. Pani, M. M. Carnasciali, J. R. Plaisier and G. A. Costa, *Inorg. Chem.*, 2016, **55**, 10567–10579.
31 S. J. Hong and A. V. Virkar, *J. Am. Ceram. Soc.*, 1995, **78**, 433–439.

